Contents lists available at ScienceDirect

Chinese Chemical Letters

Communication

Effect of carboxylic acid groups on the supercapacitive performance of functional carbon frameworks derived from bacterial cellulose

Tianyun Zhang[a,b,c], Junwei Lang[c], Li Liu[c], Lingyang Liu[c], Hongxia Li[c], Yipeng Gu[c], Xingbin Yan[c], Xin Ding[a,*]

[a] College of Textiles, Donghua University, Shanghai 201620, China
[b] School of Mechanical and Electronical Engineering, Lanzhou University of Technology, Lanzhou 730050, China
[c] Laboratory of Clean Energy Chemistry and Materials, State Key Laboratory of Solid Lubrication, Lanzhou Institute of Chemical Physics, Chinese Academy of Sciences, Lanzhou 730000, China

ABSTRACT

Three-dimensional (3D) carbonaceous materials derived from bacterial cellulose (BC) has been introduced as electrode for supercapacitors in recent. Here, we report a simple strategy for the synthesis of functional carbon frameworks through 2,2,6,6-tetramethylpilperidine l-oxyl radical (TEMPO) −mediated oxidation of bacterial cellulose (BC) followed by carbonization. TEMPO-mediated oxidation can efficiently convert the hydroxyls on the surface of BC to carboxylate groups to improve electrochemical activity. Because of its high porosity, good hydrophilicity, rich oxygen groups, and continuous ion transport in-between sheet-like porous network, the TEMPO-oxidized BC delivers a much higher gravimetric capacitance (137.3 F/g) at low annealing temperature of 500 °C than that of pyrolysis BC (31 F/g) at the same annealing temperature. The pyrolysis modified BC obtained at 900 °C shows specific capacitance (160.2 F/g), large current stability and long-term stability (84.2% of its initial capacitance retention after 10,000 cycles).

Increasing interests in developing renewable and environment friendly electrodes has driven researchers for several years [1–3]. Nanocellulose has attracted great attentions as electrode materials because of low cost, large specific surface area, high porosity and broad chemical-modification capacity [4,5]. Bacterial cellulose (BC) is one of the families of nanocellulose and it features not only common cellulosic properties but also other useful properties as ultrafine fiber network structure and rich hydrogen bonds [6]. Thus, it shows the potential applications as electrodes in electrochemical supercapacitors.

Significant efforts have been made to fabricate BC-based composite electrodes, such as carbonization [7,8], electro-deposition [9] and chemical polymerization [10]. Among these methods, one-step carbonization has shown the advantage of convenient, environment friendly and potential of large scale synthesis. For BC carbonization, the specific capacitances of electrodes prepared from pristine BC increase because of the enhanced specific surface area with the increase in carbonization temperature [7]. In this

work, we found that the specific capacitances of pyrolysis BC (p-BC) increased first and then decreased in a KOH electrolyte with the increase of carbonization temperature, exhibiting the maximum capacitance value of ∼149.1 F/g at the current density of 1 A/g at 900 °C. Further increase of the temperature above 900 °C, the specific capacitances of p-BC declined sharply. It indicates that there is a limitation to achieve higher capacitance of p-BC only through increasing the annealing temperature. On the other hand, some efforts have also been made to enhance the specific capacitance of p-BC electrodes by introducing heteroatoms into the framework [11] or combining materials with high *pseudo*-capacitance, such as metal oxides [12,13] and conductive polymers [14]. However, to the best of our knowledge, there are few reports on the surface modified-BC (MBC) and the relationship between the structure and supercapacitive performance of MBC.

Two commonly used modification methods of BC are chemical modification and bio-modification, with the former a more efficient synthetic method. *Via* chemical modification, 2,2,6,6-tetramethylpilperidine l-oxyl radical (TEMPO) −oxidized cellulose is widely used in the preparation of cellulose nanocrystals. Several reports have explored to the TEMPO-oxidized cellulose as biopolymers for "greener" electronics, such as Li/Na-ion batteries

[15,16], supercapacitors [17–19] and soft actuators [20–22]. According to those reports, the oxidized BC nanofibers framework using TEMPO under mild conditions showed good dispersibility and hydrophilicity [15,21,23], which is beneficial to synthesis BC-based nanocomposites [20,23]. The MBC, the introduction of carboxylate functional groups *via* TEMPO-oxidization on the surface of BC, provides more effective active sites and, further, enables BC-based nanocomposites with higher loading of electroactive materials with *pseudo*-capacitance [24,25]. Furthermore, carboxylic acid groups of MBC can provide abundant protons and large ion-exchange sites to enhance the absorption of ionic liquid and ion transport properties [20], which is beneficial to the electrochemical performance of MBC. Most importantly, the introduction of TEMPO oxidized only the hydroxymethyl group of polysaccharides, with no influences on the surface of hydroxide radical [26]. As results, the obtained samples have a large number of hydroxyl and carboxyl groups.

In this study, we proposed a method by using a renewable biomass of MBC as a precursor to prepare functional carbon frameworks in one simple step. We focused on studying the change of the morphology and the relationship between the structure and the electrochemical performance of pyrolysis MBC (p-MBC) under different carbonization temperatures. The obtained carbon materials are composed of carbon nanosheets and exhibited hierarchical structure with high porosity and rich oxygenated functionalities, the common features for high-performance supercapacitors. Besides, the large amount of stable oxygen-containing species and defects derived from carboxylic acid groups would be beneficial not only increasing the possibility for electrolyte diffusion into the electrode, but providing high pseudo-capacitance as well. It is demonstrated that, with a much lower annealing temperature of 500 °C, p-MBC electrode can achieve a specific capacitance of 137.3 F/g in 2 mol/L KOH aqueous electrolyte, which is comparable with that of p-BC at 900 °C annealing temperature. Thus, the proposed method opens up a new way for achieving high specific capacitance of BC as electrodes with less crucial processing conditions.

Fig. 1a is the schematic illustration of sample preparation of p-BC and p-MBC. Here, as prepared freeze-dried MBC fibril dispersions was fabricated by using the TEMPO-mediated

oxidation method and subsequent pyrolysis by facile one-step carbonization under different temperatures. BC and MBC dispersion was prepared by adding, respectively, BC and MBC (0.6 g) into deionized water (150 mL) under gentle agitation. As shown in Fig. 1b, MBC solution was homogeneously dispersed and was clear and stable because of its high zeta potential [16]. In comparison, BC solution showed grainy appearance. SEM characterization of BC and MBC shows a dense 3D porous network structure composed of numerous ultra-thin nanofibers entangle each other (Figs. 1c and d). It is seen from Fig. 1g that, the disordered amorphous region among the oxidized cellulose easily adhered each other, resulting in the formation of sheet-like porous network. Meanwhile, some small nanofibrils fractured by fiber bundles after being carboxymethylated exposed on the surface of the MBC fibers. The reason of the morphological changes is that there were a large number of hydroxyl groups on the BC chains before modification. Once the introduction of carboxyl groups, the interaction of hydrogen bond was damaged resulting in the separation of fiber bundles and reduction in fiber length [24]. In the process, the 3D network of BC became a disassembly structure and the individual fibers of the BC were densely packed again because of the existing undamaged hydrogen bond and van der Waals, forming a more flat and compact structure. XRD images of the pristine BC and MBC (Fig. 1e) displayed peaks at 14.5°, 16.9° and 22.7° of polymorph cellulose I, which is Iα-rich. This means that MBC maintained the crystallinity and did not change from the original crystal width of BC [27,28]. In addition, the thermal stability of MBC was decreased compared with that of BC (Fig. S1 in Supporting information). From the FT-IR spectra of MBC and BC (Fig. S2a in Supporting information) it is seen that most of the main bands were unchanged, with the exception of C=O vibrations shifted from at 1646 cm^{-1} to 1624 cm^{-1} (Fig. S2b), showing carboxylate groups at C6 position of the molecules by TEMPO-mediated oxidation [20,24].

After carbonization at high temperature under Argon, both the BC and MBC samples turn black, indicating a successful transformation of cellulose into carbon. In this study, the pyrolysis samples were labeled as p-BCx and p-MBCx, where the suffix "x" refers to the annealing temperature. Fig. 2 shows SEM images of p-BC500, p-BC900, p-MBC500 and p-MBC900 with low and high magnification. The morphology of p-BC500 is similar to that of p-BC900 with nanofibrils packed irregularly forming a dense porous network. Because the fibers became shorter and thicker after TEMPO-modification, the structure of p-MBC500 and p-MBC900 is quite unique, still remaining the 3D porous structure with a small number of individual nanofibers and numerous sheet-like porous network ranging from several hundreds of nanometers to mirometers. The unique structure provides not only the plenty passage of charge transfer and ion transport but also allows more active materials fully exposed to electrolytes. TEM images (Fig. S4 in Supporting information) show that p-MBC has layers and unzipped bundles microstructure, which are more flat and compact than the fibers in p-BC.

To further study the microstructure of p-BC and p-MBC, XRD and Raman spectroscopy are shown in Figs. S5 and S6 in Supporting information, respectively. All XRD patterns exhibit broad peaks at 24° and 43°, indicating the crystallographic planes of (002) and (100) in the disordered carbon structure [29]. Raman spectra in Fig. S6 give the relative intensity ratio of the D peak to G peak, I_D/I_G, that indicates the amount of defects in the graphitic structure [7,30]. The I_D/I_G values of p-BC500, p-BC700, p-BC900 and p-BC1000 are 0.65, 0.89, 1.52 and 1.31, and those of p-MBC500, p-MBC700, p-MBC900 and p-MBC1000 are 0.89, 1.06, 1.65 and 1.33. The results show that both group of p-BCx and p-MBCx has a disordered structure and there are increasing number of defects with the increase of carbonization temperature, which
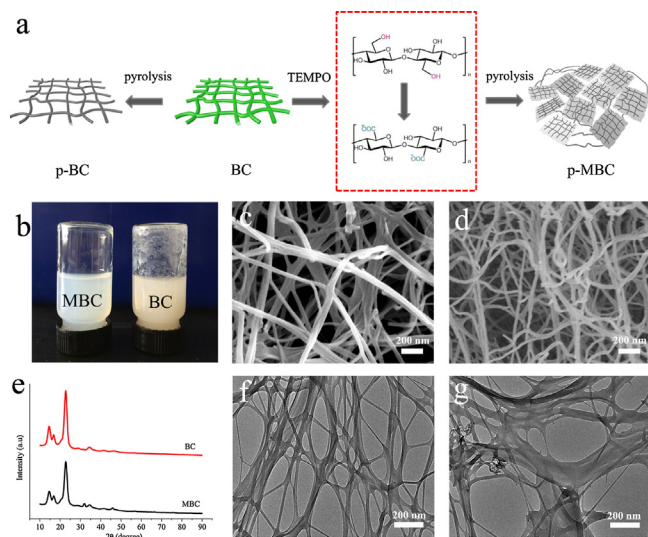

Fig. 1. (a) Schematic illustration of the preparation of p-BC and p-MBC samples; (b) Digital photos of BC and MBC suspension; Scanning electron microscope (SEM) images of (c) BC and (d) MBC; (e) X-ray diffraction (XRD) patterns of BC and MBC; Transmission electron microscopy (TEM) images of (f) BC and (g) MBC.
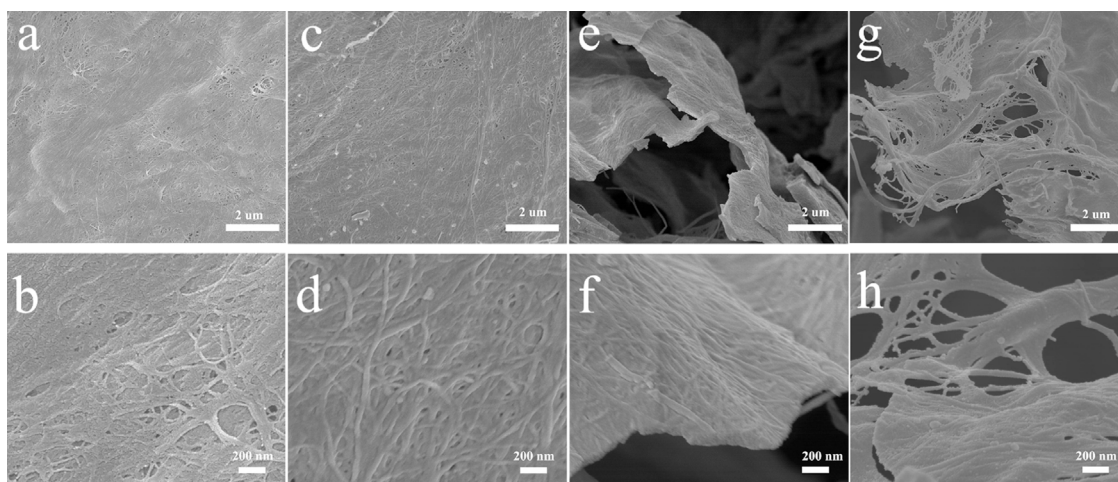
Fig. 2. (a) Low and (b) high magnification SEM images of p-BC500; (c) Low and (d) high magnification SEM images of p-BC900; (e) Low and (f) high magnification SEM images of p-MBC500; (g) Low and (h) high magnification SEM images of p-MBC900.

is beneficial for the high power output as electrode materials for supercapacitors [30].

As we know, a large accessible surface area and suitable pore size is important for the capacitivity of supercapacitors. For p-BCx, with the increase of annealing temperature, the surface area of the samples increases first and then decreases. In Fig. 3a, it is clearly observed that p-BC900 has the largest specific surface area of 487.76 m^2/g, while p-BC1000 exhibit smaller surface areas of 342.86 m^2/g. Fig. 3b shows that p-BCx displays rich porous structures that consist of a large number of mesopores, especially p-BC900. For samples of p-MBCx, the influence of annealing temperature on the specific surface area shows similar pattern as that of p-BCx (Fig. 3d). For p-MBC900, a large amount of micropores and mesopores are present, with the pore size distribution in the range of 1.4–3 nm (Fig. 3e). However, the surface area of the sample is only 198.46 m^2/g much smaller than

that of the p-BC900, the BC sample without TEMPO-oxidation. Similarly, the surface area of p-MBC500 is smaller than that of its counterpart, p-BC500. However, the former, the modified sample, owns more mesopores, which is beneficial to the electrolyte access to the electroactive sites.

To study the effect of annealing temperature on the structure evolution, specifically, the oxygen functional groups of p-BC and p-MBC, X-ray photoelectron spectroscopy (XPS) analysis shows that p-MBC and p-BC contains mainly carbon and oxygen elements (Fig. S7 in Supporting information). The O 1s can be divided into three sharp peaks from C=O (531.3 eV), C—O (532.2 eV) and O=C—O (533.2 eV) bonds [31] (Fig. 3c). Apparently, the concentration of C—O decreases with an increase in annealing temperature, while the concentration of the total of O=C—O and C=O increases. Fig. 3f reveals that the atom ratios of O/C for p-MBCx remains almost unchanged at the temperature below
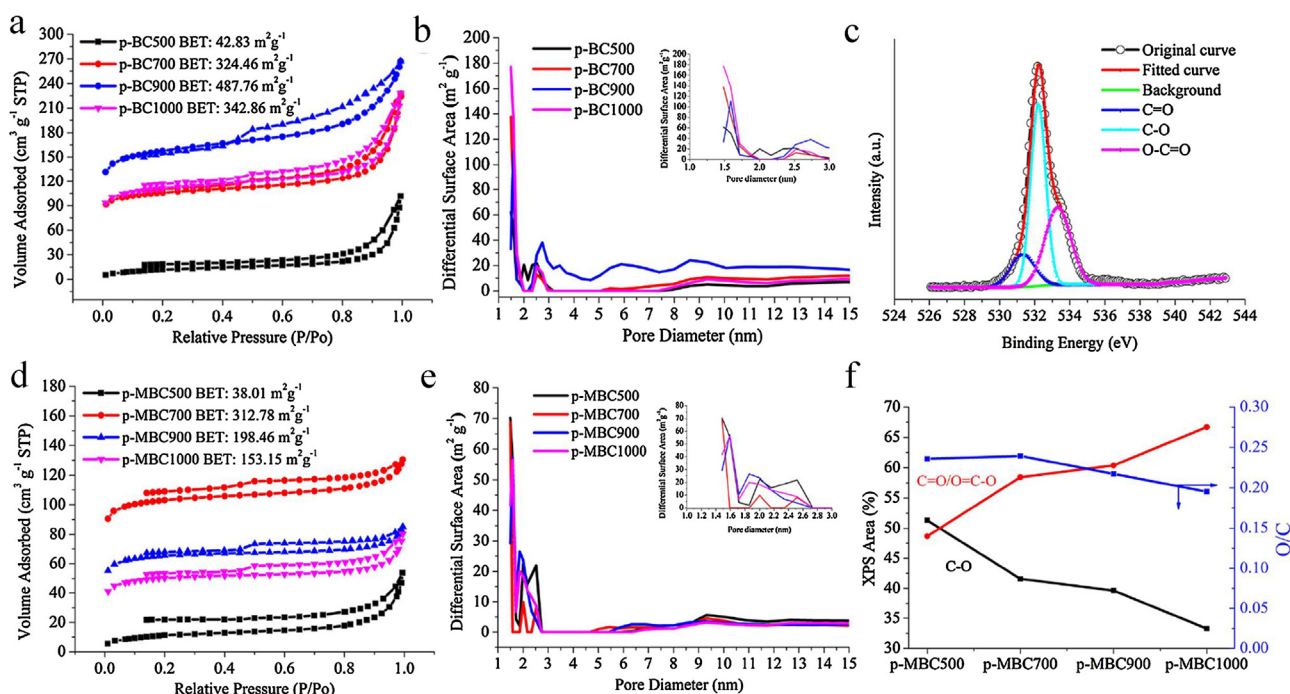

Fig. 3. (a) Nitrogen adsorption–desorption isotherms and (b) the pore size distributions of p-BCx; (c) O 1s XPS spectra of p-MBC500; (d) Nitrogen adsorption–desorption isotherms and (e) the pore size distributions of p-MBCx; (f) O/C ratio based on XPS O 1s and the variation of the amount of oxygen groups for samples.

700 °C. It demonstrates that the labile hydroxyl groups can transform to stable C=O groups.

The electrochemical performance of p-BCx and p-MBCx electrode for supercapacitors was measured in a three-electrode system with 2 mol/L KOH as an aqueous electrolyte. The results are shown in Figs. 4 and 5.

As shown in Fig. 4a, the fusiform area enclosed by the CV curves of p-BC500 at 50 mV/s is very small, and the redox peaks can hardly be observed. With a rather low value of 30.8 F/g the sample of p-BC500 does not show good performance of electrical double layer capacitive (EDLC) behavior. The reason could be attributed to the low degree of carbonization of BC sample at 500 °C, leading to the low electric conductivity and low specific surface area. With increasing carbonization temperature over 500 °C, the shape of the CV curves of p-BCx become rectangular gradually. When the annealing temperature reaches 900 °C, the sample of p-BC900 exhibits a maximum capacitance of 149.1 F/g at the current density of 1 A/g (Fig. 4b). At the high annealing temperature of 1000 °C, the capacitance value of only 115.5 F/g was obtained, although BET surface area is 342.86 m²/g. Therefore, the pore size distribution should also be considered. At 1000 °C the internal structure of p-BC changed. Both of the number of mesopores and the pore volume of p-BC1000 were decreased. The pore volume of p-BC900 is 0.40 cm³/g, while that of p-BC1000 is 0.33 cm³/g. For p-BCx, BET surface area and pore size distribution played an important role in determining the capacitance of carbonization samples in aqueous KOH electrolyte. There is no indication of faradaic reactions observed for all p-BCx samples.

For p-MBCx, it can be seen that the area enclosed by the curves of p-MBC500 is about the same as or even larger than those of other samples of p-MBCx at higher annealing temperatures (Fig. 4c). The specific capacitance of p-MBC500, p-MBC700, p-MBC900 and p-MBC1000 electrodes calculated from GCD curves (Fig. 4d) are 137.4, 149.5, 160.2 and 87.5 F/g, respectively, at current density of 1 A/g. According to Fig. 3d, the BET surface area of p-MBC1000 is much higher than that of p-MBC500, however, the capacitance of p-MBC1000 was significantly lower than those of

others. The different trends were particularly interesting because BET surface area played a significant role in determining the capacitance of p-BCx. The oxygen-containing functional group should be considered. Fig. 4c shows that the CV curve of p-MBC500 deliver a couple redox peaks at −0.7 ∼ −0.2 V, indicating the pesudocapacitive behavior of the electrode. These peaks are attributed to the redox of function groups of C=O and O—C=O according to the equation [31,32]:

$$>C-OH + OH^- = >CO^- + H_2O \qquad (1)$$

$$>C=O + OH^- = >COOH + e^- \qquad (2)$$

$$-COOH + OH^- = -COO^- + H_2O \qquad (3)$$

With the increasing temperature of carbonization, the atom ratios of O/C decreased (Fig. 3f), and the disappeared peak around −0.8 V, indicates that oxygen-containing groups are brought in the additional *Pseudo*-capacitance in aqueous KOH electrolyte.

Both p-BCx and p-MBCx display highly porous structures that consist of a large number of micropores and mesopores. Compared to p-BCx, the capacitance of p-MBCx also increased first and then decreased with an increase of annealing temperature, but with some different characteristics, especially for p-BC500 and p-MBC500. Although the BET surface area of p-MBC500 is smaller than that of p-BC500, the capacitance of the former is larger than that of the latter. As shown in Fig. 5a, the area enclosed by the CV curves of p-BC500 at 10 mV/s is very small and the redox peaks can hardly be observed. By comparison, that of p-MBC500 is much larger and the curves display a broad peak around −0.7 V, which could be attributed to the *pseudo*-capacitive contribution from the redox reactions of the oxygen-containing functional groups on the surface of p-MBCs [33]. The amount of functional groups on the surface of p-MBC500 are more than that of p-BC500 (Fig. S9 in Supporting information), and the atom ratios of O/C for p-BC500 (0.23) are lower than that for p-MBC500 (0.24). The increase in the
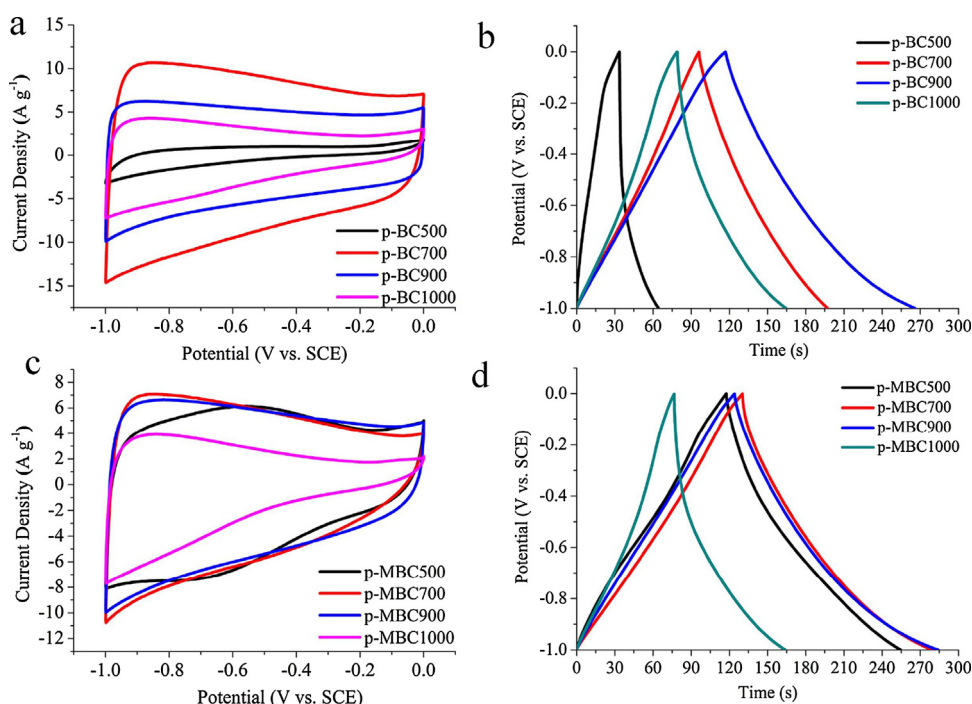

Fig. 4. (a) CV curves of the p-BCx electrode at 50 mV/s; (b) Galvanostatic charge/discharge curves of p-BCx electrode at current density of 1 A/g; (c) CV curves of the p-MBCx electrode at 50 mV/s; (d) Galvanostatic charge/discharge curves of p-MBCx electrode at current density of 1 A/g.
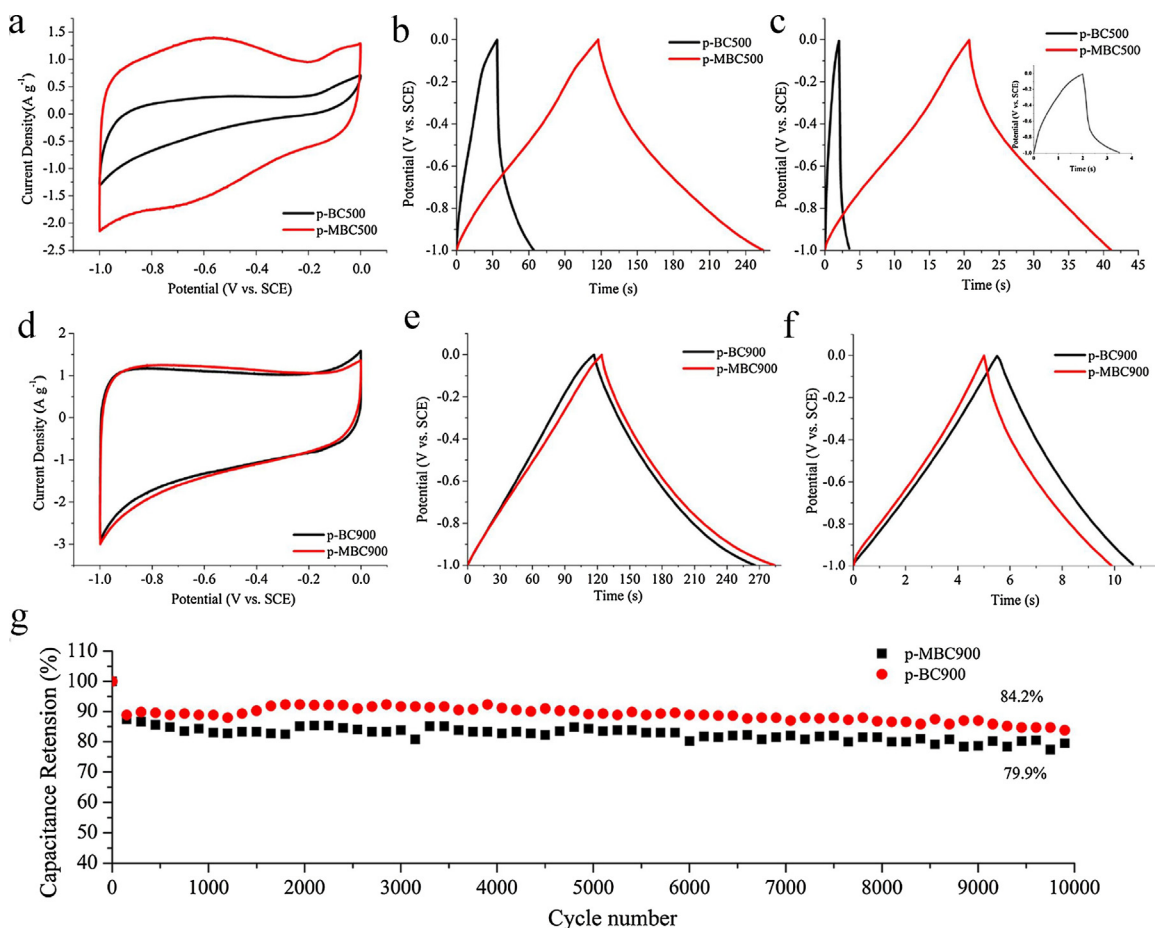
Fig. 5. (a) CV curves of p-BC500 and p-MBC500 electrode at 10 mV/s, (b) Galvanostatic charge/discharge curves of p-BC500 and p-MBC500 electrode at current density of 1 A/g; (c) Galvanostatic charge/discharge curves of p-BC500 and p-MBC500 electrode at current density of 5 A/g; (d) CV curves of p-BC900 and p-MBC900 electrode at 10 mV/s, (e) Galvanostatic charge/discharge curves of p-BC900 and p-MBC-900 electrode at current density of 1 A/g; (f) Galvanostatic charge/discharge curves of p-BC900 and p-MBC900 electrode at current density of 20 A/g; (g) Cycling performance of p-BC900 and p-MBC900 electrode at current density of 1 A/g.

functional groups of p-MBC500 not only increase the wettability between electrolyte and the electrode [34], but also provides pseudo-capacitance. Therefore, the pseudo-capacitance form oxygen-containing functional groups on the surface of p-MBC500 makes a major contribution to the capacitance of the electrode. Besides, the I_D/I_G values increase from 0.65 of p-BC500 to 0.89 of its TEMPO-oxidized counterpart, p-MBC500, suggesting that there are more defects generated in the latter, which is beneficial for the accumulate charges and charge transfer due to more accessible surface area [7]. From the above reasons, they suggest that the p-MBC500 displays both EDLC behavior and pseudo-capacitance performance.

According to the comparison of CV and GCD curves, p-MBC900 and p-BC900 displays the prominent electrochemical capacity among them. As expected, the charge and discharge curves (Figs. 5e and f) are symmetric, indicating a high reversibility of the reaction of p-MBC900 and p-BC900. For p-MBC900 sample, large accessible surface area and suitable pore size would facilitate electrolyte to enter into the pore and enabled the formation of EDLC to store the charge. The results suggested that increasing BET surface area and pore size both had a significant influence on the capacitance value for p-MBC900. Therefore, p-MBC900 shows a typical electrical double layer capacitive behavior.

In addition to the high specific capacitance, the rate capability and cycle stability should also be considered as important factors for ideal supercapacitors. For p-BC900 and p-MBC900, voltage drops are hardly observed at high current density of 20 A/g (Fig. 5f).

However, voltage drops of p-BC500 and p-MBC500 are very distinct even at a current density of 5 A/g (Fig. 5c). It indicates that the p-BC900 and p-MBC900 have good rate capacities with higher carbonization temperature. Additionally, the CV curve of p-BC900 retained its rectangular shape even at 700 mV/s (Fig. S8a in Supporting information), while that of p-MBC900 could hardly keep the rectangular shape when the scan rate was as low as 200 mV/s (Fig. S8b), indicating a better rate electrochemical performance of the p-BC900 electrode. The specific capacitance of the samples calculated based on the CV curves can be observed in Fig. 6a, while those based on the GCD curves in Fig. 6b. The p-MBC700 electrode exhibits high gravimetric capacitance of 127.6 F/g at 10 mV/s, while the p-MBC900 electrode presents
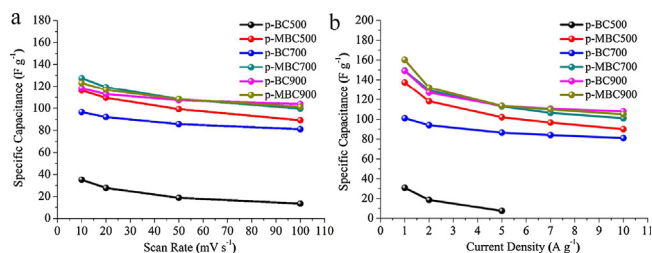

Fig. 6. Comparison of gravimetric specific capacitances of p-BC500, p-MBC500, p-BC700, p-MBC700, p-BC900 and p-MBC900 _versus_ (a) scan rates, and (b) current densities.

123.1 F/g at 10 mV/s. At high scan rate up to 200 mV/s, the gravimetric capacitance of p-MBC900 is slightly higher than that of p-MBC700, indicating rate capability as the carbonization temperature rises. As shown in Fig. S10a in Supporting information, the equivalent series resistance of p-BC500 ($\approx 0.89\,\Omega$) is lower than that of p-MBC500 ($\approx 0.95\,\Omega$), however, the straight line with the real axis angle of p-BC500 is larger than that of p-MBC500 in the low frequency, suggesting that the diffusion impedance of p-MBC500 is larger. According to Fig. S10b, it shows that the equivalent series resistance of p-BC900 and p-MBC900 are lower than the samples obtained at 500 °C, suggesting very low resistance and good ion response. So the cycling test of p-BC900 shows 84.2% of capacitance retention over 10000 cycles at 1 A/g (Fig. 5g), demonstrating good electrochemical stability. Compared with the previous reported carbon based supercapacitors in aqueous electrolyte, p-BC900 and p-MBC900 show outstanding electrochemical performance (Table S1 in Supporting information).

In conclusion, samples of p-MBC were successfully synthesized from BC pellicles through a TEMPO-mediated oxidation and subsequent carbonization. For p-BCx, the high BET surface area and rich mesopores are beneficial to form EDLC to enhance the capacity and rate capability. For p-MBCx, the oxygen-containing functional groups introduce the extra pseudo-capacitance. The p-MBC electrode at 500 °C possesses a high specific capacitance of 137.3 F/g in 2 mol/L KOH aqueous electrolyte with excellent rate capability, which is much higher than the pristine BC under the same annealing temperature. The results show that p-MBC500 displays both electrical EDLC behavior and pseudo-capacitance performance, and the effect of the functional groups is the dominant factor for the capacitance of p-MBC500. In addition, p-MBC pyrolysis at 900 °C also shows specific capacitance (160.2 F/g), rate performance and long-term cycling stability in 2 mol/L KOH aqueous electrolyte. This work provides a simple and effective method to prepare hierarchical structure nanosheets with stable oxygen functional groups and rich pore structure, which beneficial for the high capacitance, rate capability and cycling stability. These findings promote the design for BC as electrode material for supercapacitors and other energy-storage devices such as Na-ion batteries, Li-ion batteries and Li–S batteries.

Materials: Bacterial cellulose (BC) was purchased from Hainan Yida Food Industry Co., Ltd., China. 2,2,6,6-Tetramethylpiperidine-1-oxyl radical (TEMPO) was obtained from Sigma-Aldrich. Sodium hypochlorite (NaClO), sodium bromide (NaBr), ethanol and sodium hydroxide (NaOH) were purchased from Lanzhou Zhongke Kate Equipment Distribution Co., Ltd.

Preparation of MBC and BC: BC pellicles were first cut into small pieces and pulped with a mechanical stirring. The obtained mixture was freeze-dried. The MBC was fabricated using the TEMPO oxidation method [20–22].

Fabrication of p-MBC and p-BC: The as-prepared BC and MBC was pyrolyzed at 500 °C, 700 °C, 900 °C and 1000 °C in a horizontal tube furnace for 2 h with a heating rate of 5 °C/min in Argon. After cooling down to room temperature, the samples were washed with deionized water several times, and dried at 60 °C overnight in a vacuum oven.

Characterization: The morphology and the structure of p-BCx and p-MBCx was characterized by a field emission scanning electron microscopy (FESEM, JSM 6701F) and a transmission electron microscopy (TEM, JEOL 2100 FEG). The chemical components were measured by an X-ray photoelectron spectrometer (XPS, ESCALAB250x). The thermal stability of the samples was characterized by thermo-gravimetric analysis (STA449C) at a rate of 10 °C/min under air atmosphere from room temperature to 800 °C. The nitrogen adsorption-desorption isotherm measurements were performed on an ASAP 2020 volumetric adsorption

analyzer (Micromeritics, USA) at 77 K. Powder X-ray diffraction (XRD, Rigaku D/Max-2400, Cu–Kα radiation, $\lambda = 0.15405$ nm). Raman spectroscopy (Horiba Jobin Yvon HR Evolution) and Fourier transform infrared spectroscopy (FTIR, IFS120HR) were employed to investigate the microstructure of the as-prepared samples.

Electrochemical measurements: All electrochemical tests were carried out in a three electrode testing system (CHI 660D electrochemical workstation, Shanghai) with a platinum electrode as a counter electrode and a saturated calomel (SCE) electrode as a reference electrode. The mixture of active material, acetylene carbon and polytetrafluoroethylene (PTFE) binder with a mass ratio of 80:10:10 was coated onto the nickel foams (about 1 mg of active material) under the pressure of 10 MPa and dried at 60 °C for 12 h in a vacuum oven.

Cyclic voltammetry (CV), Galvanostatic charge-discharge (GCD) and Electrochemical impedance spectroscopy (EIS) test were measured in 2 mol/L KOH aqueous electrolyte. The CV was carried out over the potential range of −1 V to 0 V. The EIS measurements were carried out at an open circuit potential with a frequency range from 0.01 Hz to 100 kHz. The long-term cycling stability was assessed according to GCD with a potential range between −1 V and 0 V for 10000 cycles.

The specific capacitance was calculated according to the GCD curve [35]:

$$C = I / \left[\left(\frac{dV}{dt}\right)m\right] \approx \frac{I\triangle t}{m\triangle V}(F/g) \tag{1}$$

Where I is the discharge current (A), Δt is the discharging time (s), m is the mass of active materials (g), and ΔV is the voltage drop upon discharge (excluding the IR drop) (V).

The specific capacitance (C) according to the CV curve [30]:

$$C = \left(\int I\mathrm{d}V\right)/vmV \tag{2}$$

Where I is the current density, V is the potential window, v is the potential scan rate, and m is the mass of the active materials.

Acknowledgment

Appendix A. Supplementary data

Supplementary data associated with this article can be found, in the online version, at http://dx.doi.org/10.1016/j.cclet.2017.08.013.

References

[1] H. Khalil, A.H. Bhat, A.F.I. Yusra, Carbohydr. Polym. 87 (2012) 963–979.
[2] T.H. Nguyen, A. Fraiwan, S. Choi, Biosens. Bioelectron. 54 (2014) 640–649.
[3] X.H. Lu, M.H. Yu, G.M. Wang, et al., Energy Environ. Sci. 7 (2014) 2160–2181.
[4] D. Klemm, F. Kramer, S. Moritz, et al., Angew. Chem. Int. Ed. 50 (2011) 5438–5466.
[5] K. Shi, X. Yang, E.D. Cranston, et al., Adv. Funct. Mater. 26 (2016) 6437–6445.
[6] X. Chen, F. Yuan, H. Zhang, et al., J. Mater. Sci. 51 (2016) 5573–5588.
[7] Y. Liu, T. Lu, Z. Sun, et al., J. Mater. Chem. A 3 (2015) 8693–8700.
[8] L.F. Chen, Z.H. Huang, H.W. Liang, et al., Energy Environ. Sci. 6 (2013) 3331–3338.
[9] S.H. Li, D.K. Huang, B.Y. Zhang, et al., Adv. Energy Mater. 4 (2014) 7–10.
[10] H.H. Wang, L.Y. Bian, P.P. Zhou, et al., J. Mater. Chem. A 1 (2013) 578–584.
[11] L.F. Chen, Z.H. Huang, H.W. Liang, et al., Adv. Funct. Mater. 24 (2014) 5104–5111.
[12] L.F. Chen, Z.H. Huang, H.W. Liang, et al., Adv. Mater. 25 (2013) 4746–4752.
[13] L.Y. Liu, X. Zhang, H.X. Li, et al., Chin. Chem. Lett. 28 (2017) 206–212.
[14] C. Long, D. Qi, T. Wei, et al., Adv. Funct. Mater. 24 (2014) 3953–3961.

[15] H. Lu, M. Behm, S. Leijonmarck, et al., ACS Appl. Mat. Interfaces 8 (2016) 18097–18106.
[16] F. Shen, H. Zhu, W. Luo, et al., ACS Appl. Mater. Interfaces 7 (2015) 23291–23296.
[17] F. Wang, H.J. Kim, S. Park, et al., Compos. Sci. Technol. 128 (2016) 33–40.
[18] Z. Wang, D.O. Carlsson, P. Tammela, et al., ACS Nano 9 (2015) 7563–7571.
[19] Q.Z. Liu, S.S. Jing, S. Wang, et al., J. Mater. Chem. A 4 (2016) 13352–13362.
[20] S.S. Kim, J.H. Jeon, H.I. Kim, et al., Adv. Funct. Mater. 25 (2015) 3570.
[21] F. Wang, J.H. Jeon, S.J. Kim, J. et al, Mater. Chem. B 4 (2016) 5015–5024.
[22] F. Wang, J.H. Jeon, S. Park, et al., Soft Matter. 12 (2016) 246–254.
[23] Y. Jia, X. Zhai, W. Fu, et al., Carbohydr. Polym. 151 (2016) 907–915.
[24] L.N. Yue, Y.D. Zheng, Y.J. Xie, et al., RSC Adv. 6 (2016) 68599–68605.
[25] B. Bideau, L. Cherpozat, E. Loranger, et al., Ind. Crop Prod. 93 (2016) 136–141.
[26] W.N. Ren, W.W. Zhou, H.F. Zhang, et al., ACS Appl. Mater. Interfaces 9 (2017) 487–495.
[27] W. Fan, K. Si-Seup, K. Chang-Doo, et al., Smart Mater. Struct. 23 (2014) 074006–074016.
[28] W. Hu, S. Chen, X. Li, et al., Mater. Sci. Eng. C 29 (2009) 1216–1219.
[29] X.L. Zhu, P.Y. Wang, C. Peng, et al., Chin. Chem. Lett. 25 (2014) 929–932.
[30] D.D. Shan, J. Yang, W. Liu, et al., J. Mater. Chem. A 4 (2016) 13589–13602.
[31] L.L. Jiang, L.Z. Sheng, C.L. Long, et al., Adv. Energy Mater. 5 (2015) 771–780.
[32] Y. Qiu, H. Dang, Z. Cheng, et al., Ionics 22 (2016) 529–534.
[33] Q. Liang, L. Ye, Z.H. Huang, et al., Nanoscale 6 (2014) 13831–13837.
[34] B.S. Shen, H. Wang, L.J. Wu, et al., Chin. Chem. Lett. 27 (2016) 1586–1591.
[35] L. Liu, J.W. Lang, P. Zhang, et al., ACS Appl. Mat. Interfaces 8 (2016) 9335–9344.